**Article:**
Yue, X, Zhang, L, Wang, Y et al. (5 more authors) (2020) Evolution and characterization of the film formed on super 13Cr stainless steel in CO2-saturated formation water at high temperature. Corrosion Science, 163. 108277. ISSN 0010-938X

https://doi.org/10.1016/j.corsci.2019.108277

# *Evolution and characterization of the film formed on super 13Cr stainless steel in $CO_2$-saturated formation water at high temperature*

Xiaoqi Yue[a], Lei Zhang[a], Yun Wang[a], Shusheng Xu [b], Chun Wang[b], Minxu Lu[a], Anne Neville[b] and Yong Hua[b]*

a: Institute of Advanced Materials and Technology, University of Science and Technology Beijing, 30 Xueyuan Road, Beijing, 100083, China.
b: Institute of Functional Surfaces, School of Mechanical Engineering, University of Leeds, Leeds, LS2 9JT, United Kingdom.

*Corresponding author: Yong Hua, Tel: +44 (0) 7923359918, fax: +44 (0) 1132424611.
Email: Y.Hua@leeds.ac.uk

## *Abstract*:

The evolution and characterization of films formed on super 13Cr at 90°C and 200°C were investigated by Scanning Electron Microscopy (SEM), X-Ray Diffraction (XRD), X-Ray Photoelectron Spectroscopy (XPS), Focus Ion Beam (FIB) and Transmission Electron Microscopy (TEM) and localized Raman spectroscopy. The results show that super 13Cr maintains a passive state at 90°C, while an active state exists with a high corrosion rate of 0.43 mm/year at 200°C for the first 5 hours, then stabilizes to a rate of 0.125 mm/year over 5 days exposure. The passive film formed at 90°C is an amorphous-like structure with high Cr content, while the corrosion product films formed at 200°C are mainly comprised of nanocrystalline spinel $FeCr_2O_4$ and crystalline $FeCO_3$.

Keywords: super 13Cr stainless steel, FIB-TEM, $CO_2$ corrosion, scale film

## *Introduction*

Stainless steels contain high levels of passivating elements such as chromium, molybdenum, and nickel, resulting in excellent corrosion resistance [1]. Generally the corrosion resistance increases with increasing chromium content: duplex stainless steels (18-28Cr) > austenitic stainless steels (18Cr) > martensitic stainless steels (11.5-18Cr). A common cost-effective material for downhole injection or production tubing is 13Cr stainless steels (UNS S41000) due

to their mechanical properties and economic applicability [2]. However, normal 13Cr is susceptible to corrosion when the temperature reaches 150°C. Recently, the potential material is known as super 13Cr (UNS S41427) containing approximately 5% Ni has been shown to improve corrosion resistance compared to normal 13Cr at higher temperature. Super 13Cr can provide more cost-effective performance compared to Corrosion Resistant Alloys (CRAs) such as 22Cr and 25Cr duplex stainless steel. Therefore, super 13Cr stainless steels with a martensitic microstructure have been widely used in oil and gas containing $CO_2$ environments [3,4].

It is well known that stainless steel has excellent corrosion resistance because the passive film can act as a barrier to restrict the corrosive species contacting the surface [5]. Previous research has found that no differences in composition and thickness exist between passive films formed at room temperature and at 90$^{o}$C in a 0.5 M NaCl solution [6]. In an acidic environment, the outer region of the passive film normally consists of a layer enriched in iron-based on a transfer artefact related to the higher diffusion rate of iron, while the inner layer is strongly enriched in chromium caused by the dissolution of iron [7,8]. The work done by Zhang et al. [9] reported that 13Cr surface has passivation abilities at 90 °C; the primary component of the passive film was $Cr_2O_3$. Lee et al. [10] indicated that the passive film can increase in thickness by the additional Cr content in the material, results in improved corrosion resistance by effectively blocking the surface and reducing in the number of film defects. Super 13Cr has improved corrosion resistance by reducing the C content and adding 2% Mo and 5% Ni content relative to the 13Cr [11]. The extra 2% Mo in super 13Cr is effective in stabilizing the passive film in the $CO_2$ environment and assists the formation of the Cr oxide passive film in the inner layer [12,13]. The Ni is enriched underneath the oxide in the bulk due to preferential oxidation of iron and chromium at the oxide/metal interface [14], which limits the rate at which Cr is available for the formation of $Cr_2O_3$ [15].

From previous research, it has been found that the thickness of the film reaches the micron-scale at 150$^{o}$C on super 13Cr surfaces after 30 days exposure [16], in comparison to the film formed at temperatures of 120°C or below which is orders of magnitude thinner. Zhang et al. [9] proposed that the surface films may comprise both $Cr_2O_3$ and $FeCO_3$ at 150 °C. Mu et al. [17] illustrated that the outer iron oxides and hydroxides in passive films can be destroyed in

the stratum water with the temperature rising from 30°C to 90°C, and iron/chromium oxides and $FeCO_3$ become the major components of the corrosion scales formed at 90°C with saturated $CO_2$. In the context of oil and gas production, the service temperature of tubing in the bottom of ultra-deep well is much higher than these well-studied temperature ranges. Moreira et al.[18] indicated the Cr-enrichment in corrosion product layer was more pronounced with an increase in temperature from 125°C to 175°C. Zhao et al. [19] combined the Pourbaix diagrams and surface analyses to explore the composition of corrosion products for super 13Cr in the $H_2O$-$Cl^-$-$CO_2$ aggressive oilfield environment up to 180°C. It showed that the content of $Cr_2O_3$ decreased with increase in temperature and pressure; their results indicated that the corrosion product film can be regarded as an unstable structure and it would reduce protectiveness of scales and pitting resistance. Besides, they found the formation of corrosion product films on super 13Cr at high temperature involved precipitated $Cr_2O_3$ and $Cr(OH)_3$, and the existence of $Cr_2O_3$/$Cr(OH)_3$ phase boundary which may cause higher defect density [20]. In February 2019, more than 100 billion cubic meters of natural gas was discovered from Bohai in China. The pipeline materials ~~are~~ exposed to an aggressive geological environment with temperatures to 200°C.

Since the mid-20th century, numerous attempts to model film growth based on different concepts have been made. Among them, a widely recognized model has been the Point Defect Model (PDM) proposed by Macdonald [21]. According to the PDM, the passive film generally comprises a bilayer structure consisting of a defective oxide layer that grows directly into the metal and a precipitated outer layer that forms via the hydrolysis of cations ejected from the inner layer. In HTHP $CO_2$ conditions, however, there are still some questions on the application of PDM. Research studies have indicated that the passive film formed at temperatures below 100°C is mainly an outer precipitated layer ($Cr(OH)_3$) and the inner oxide layer ($Cr_2O_3$) [20]. On the other hand, for the context of oil and gas production, precipitated $FeCO_3$ should also be considered once the presence of $Fe^{2+}$ and $CO_3^{2-}$ reach the supersaturation ratio [22]. Guo et al. [23] found that the crystalline state of $FeCO_3$ was determined by chromium hydrolysis, which means amorphous-like $FeCO_3$ and microscale $FeCO_3$ crystalline grains would be observed in different corrosion stages. For the early $Cr(OH)_3$ film-forming stage, the pH value on the matrix surface would be much lower than the stage after the formation of the film [24],

causing the changes in the state of thermodynamics. Besides, with the high temperature for prolonged periods, some small unripened $FeCO_3$ would transform into other products without oxygen in proper thermodynamic circumstances [25,26].

The corrosion behaviour of super 13Cr and the formation mechanism of the corrosion product scales studies are rare at 200$^{o}$C. It is obvious that the formation of passive film or corrosion product film on the surface at high temperature is complex. The evolution and film growth is essential to understanding the nature of the film in terms of corrosion product kinetics and protective capability in HTHP environments. No work has been done with super 13Cr at high temperature and to focus on the presence of Ni and the relationship between corrosion product growth at various immersion times and in-situ corrosion rate measurements. This research work investigates the knowledge gap for super 13Cr stainless steel exposed to high temperature $CO_2$ environments. The corrosion behaviour and corrosion product formation mechanism of super 13Cr over 120 hours in $CO_2$-saturated 4.86 wt.% NaCl solution at 90°C and 200°C simulates the deep well environment in Bohai. The chemical composition of the corrosion product, the morphology and their evolution formed on the surface are analysed at 5, 14, 29, 48 and 120 hours by a combination of SEM/EDX, XRD, XPS, Raman spectroscopy and FIB/TEM and related to the level of protective capability.

## *Experimental*

### *2.1. Material and methods*

The test material used was an API-P110 grade super 13Cr stainless steel supplied by Bao Steel from China with a chemical composition (wt%): C 0.041%, Si 0.34%, Mn 0.34%, Cr 12.80%, Mo 1.92%, S ≤0.001%, P ≤0.001%, Ni 4.78% and Fe balance. The material was heat-treated through normalization and tempering at 980°C and 590°C, respectively. Coupon specimens with a dimension of 30 mm × 13 mm × 3 mm were used for immersion tests. The cylinder-shaped specimens with a hole (7 mm diameter) for electrochemical measurement were machined with dimensions of 21 mm in diameter and 7 mm in length. The electrodes for electrochemical measurement were embedded in polyetheretherketone (PEEK) with an exposed working area of 461.8 mm$^2$, as shown in Fig.1b. Prior to each test, the specimens were ground to 1200 grit using silicon carbide paper, then rinsed with deionized water,

acetone and dried. All tests were performed at 90°C and 200°C with a $CO_2$ partial pressure of 2.8 bar. And the volume to surface ratio was kept at approximately 33 ml/cm$^2$.

***Corrosion rate measurements***

Two evaluation methods, weight loss method, and LPR (Linear Polarization Resistance) method were used in this study. Among them, the weight loss method is generally believed to have high accuracy but only obtains an average corrosion rate. The in-situ LPR method is used to determine the instantaneous polarisation resistance ($R_p$) tendency as a function of time, as inaccurate Tafel constants for stainless steel limits the determination of the exact degradation rates for this system. ~~Therefore, it is better to compare both methods in order to obtain corrosion rates at various immersion times.~~ The $1/R_p$ trends is presented as a semi-quantitative values of the trends of corrosion rates in these extreme conditions.

Test solutions to simulate the formation water from a gas field were made from analytical grade reagents and deionized water. The chemical composition is shown in Table 1.

Table 1. Chemical composition of the formation water

| Composition | $Na^+$ | $Cl^-$ | $HCO_3^-$ |
|---|---|---|---|
| Content (mg/L) | 19335 | 29503 | 585 |

A C-276 alloy static autoclave was utilized to conduct all the weight loss or LPR tests as schematically shown in Fig. 1a. For mass loss experiments, three coupons were mounted on a designed PEEK holder and fully immersed in the test solution. The solution was de-aerated by saturating the 4.86 wt.% NaCl solution with $CO_2$ in a separate container overnight prior to testing. All lines to the autoclave were purged with high pressure $CO_2$ and evacuated to ensure removal of $O_2$ within the system. The prepared, $CO_2$-saturated brine (650 ml) was carefully transferred from the sparging vessel into the closed autoclave containing the test specimens at ambient pressure and temperature using a shoe suction pump (the test temperature and pressure were controlled and monitored by using a temperature controller and pressure gauge). The solution was then heated to the desired temperature.

The experimental matrix for this study is provided in Table 2. The initial pH for the $CO_2$-

saturated brines prior to heating in each experiment was 5.6 and was achieved through the addition of $NaHCO_3$. The starting solution pH at the elevated temperatures and $CO_2$ partial pressures were predicted using the commercially available OLI software package [27] and are provided in Table 2. The volume of the autoclave is 1 litre. In order to ensure the liquid-gas ratio unchanged, 650 ml of prepared solution was introduced to the autoclave. OLI software uses a Mixed Solvent Electrode (MSE) model with the extension in $CO_2$-containing systems to calculate pH value with multiple solvents and solutes at a wide ranges of pressure and temperature [28,29]. A detailed summary of the MSE model and the introduction of parameters is given by Springer et al. [30].

Table 2. Test matrix for corrosion tests under various condition

| Temperature (°C) | $CO_2$ pressure measured at 25°C (bar) | Calculated pH | Measured $CO_2$ partial pressure (bar) | Measured total pressure (bar) | Time duration (hours) |
|---|---|---|---|---|---|
| 90 | 1 | 6.01 | 1.3 | 1.9 | 48 |
| | | | | | 120 |
| 200 | | 6.41 | 2.7 | 18 | 5 |
| | | | | | 14 |
| | | | | | 29.5 |
| | | | | | 48 |
| | | | | | 120 |

Before the test, the original weight ($W_0$) of the coupon was measured using an analytical balance with an accuracy of $10^{-5}$ g. After the test, the corroded coupons extracted from the autoclave was rinsed with DI-water, dried, and weighed to get the post-test weight ($W_1$). The corrosion products were removed by using a chemical cleaning procedure suggested in ASTM G1-03 standard (Designation C.3.1) [31]. After the removal, the specimens were rinsed and dried, then weighed to obtain the final weight ($W_2$). The corrosion rate ($C_R$) was reported in mm/year according to the obtained weight loss via Eq. (1).

$$C_{\mathrm{R}} = \frac{87600(W_0 - W_2)}{t\rho A} \quad (1)$$

Where $t$ represents the immersion time, h; $\rho$ is steel density, g/cm$^3$; and A is exposed surface area in cm$^2$.

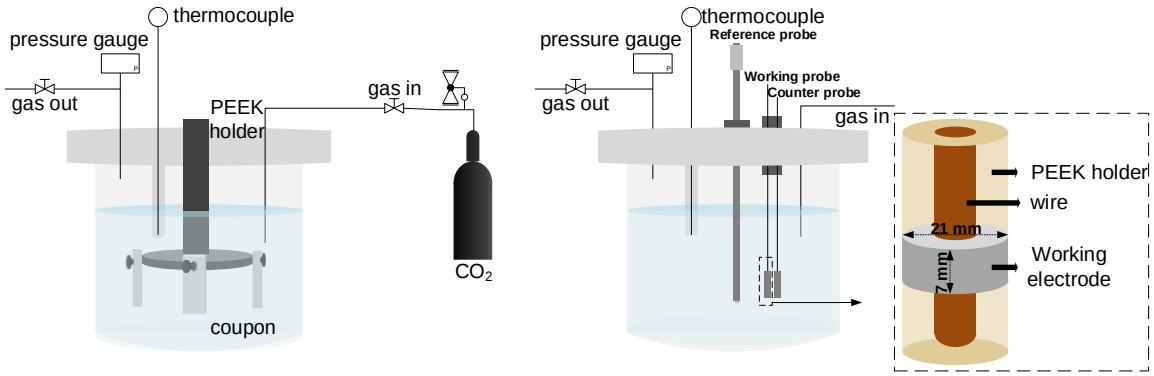


Figure 1. Schematic diagram of the high temperature and high pressure autoclave and the location of (a) mass loss samples, (b) LPR sample.

In-situ electrochemistry was used to measure the polarisetion resistance values. The electrochemical tests were measured using a three electrodes cell with a super 13Cr specimen as working electrode (WE), a platinum sheet as the counter electrode (CE) and a Ag/AgCl pressure balanced external electrode (0.1 mol/L KCl solution) as the reference electrode (RE). All electrode potentials in the present work have been converted to the standard hydrogen electrode (SHE) according to the following relationship [32]:

$$E_{\mathrm{SHE}} = E_{\mathrm{Ag/AgCl}} + 0.2866 - 0.001(T - T_0) + 1.754 \times 10^{-7}(T - T_0)^2 - 3.03 \times 10^{-9}(T - T_0)^3 \quad (2)$$

Where $E_{\mathrm{SHE}}$ is the electrode potential vs SHE, while $E_{\mathrm{Ag/AgCl}}$ is the electrode potential vs Ag/AgCl RE. $T$ represents the experimental temperature and $T_0$ represents 25 °C.

In LPR tests, the super 13Cr WE was polarized from -10 mV to +10 mV vs Open Circuit Potential (OCP) and scan rate was 0.1667 mV/s using an Ivium electrochemical workstation. When applying this method, the E vs. I curve was found to obey a good fit to a linear relationship and the results of independent experiments showed good reproducibility. The instantaneous $R_p$ values is determined from the slope of the current-potential curve:

$$R_{\mathrm{p}} = \frac{\Delta \mathrm{E}}{\Delta \mathrm{I}} \quad (3)$$

$1/R_p$ is presented as a semi-quantitave value of corrosion rate in order to prevent any inaccuracies brought about throught impleetation of Tafel constant which were not accurately determined in these condtions.

### *1.2. Surface analysis*

SEM was carried out on samples using a Carl Zeiss EVO MA15 SEM to assess coverage and morphology observation of the film formed on super 13Cr stainless steel. All images were collected at an accelerating voltage of 20 kV via secondary electron (SEI) for morphological, and back-scattered electron (BSD) for cross-section features at different time. Further, the composition variety for each sample at different time was conducted via XRD spectrum using a PANalytical X'pert multipurpose diffractometer (MPD), employing Cu Kα radiation with an active area of 10 mm × 10 mm, with a range of $2\theta$ = 20–80° using a step size of 0.033° per second. A combination of Raman spectroscopy (488 nm radiation) with an Ar ion laser and XPS with a monochromatic X-ray source (a Al kα electrode at 15 kV and 150 W) were used to identify the nature of corrosion products locally on the surface. Raman spectra were collected by employing 488 nm radiation from an Ar ion laser (1% and 5%). The exposure time for each Raman sample was recorded with a total scan time of approximately 10–50 min, while the sputtering time for each XPS sample was controlled in 1 hour, with a sputtering speed of 10 nm/h.

TEM was also performed in order to study the formation of films on the surface at 90°C and 200°C. Samples were prepared using a focused ion beam (FIB). The instrument used was an FEI Nova200 dual beam SEM/FIB fitted with a Kleindiek micromanipulator for in situ lift-out. The ion beam was operated at voltages between 30 and 5 kV, and with beam currents between 5 and 0.1 nA. Regions of interest were first coated with a protective layer of platinum before bulk removal of material was performed. Samples were then lifted out in-situ and attached to a Cu TEM grid and thinned to a final thickness of around 100 nm. TEM was performed using an FEI Tecnai F20 FEGTEM (200 kV) fitted with a high angle annular dark-field (HAADF) detector and a Gatan Orius SC600 CCD camera.

## *Results and discussion*

### *3.1. Corrosion rates from the mass loss and linear polarization measurements*

Fig. 2 shows the corrosion rates determined by weight loss and the polarisation resistance tendency of super 13Cr stainless steel exposed to $CO_2$-saturated 4.86 wt.% NaCl at 90°C and 200°C with $CO_2$ partial pressure of 1.3 bar and 2.7 bar respectively for different immersion

times determined from mass loss and LPR methods. It can be seen that the corrosion rates were low at 90°C; maintaining approximately 0.004 mm/year during the 120 hours exposure. The corrosion rates were high (0.43 mm/year) at the temperature of 200°C for the first 5 hours. For longer tests, the corrosion rate reduced and was maintained at 0.125mm/year after 120 hours.

The stable low corrosion rates at 90°C over 120 hours are attributed to the presence of a passive film on the super 13Cr surface. However, the corrosion rates for super 13Cr exposed to 200°C were high and the reduction in corrosion rates over the immersion time can be explained by the formation of protective corrosion product films as these layers slow down the corrosion processes on the surface. The next sections investigate the corrosion product compositions and morphology in order to understand the corrosion mechanism and film evolution on the surface.

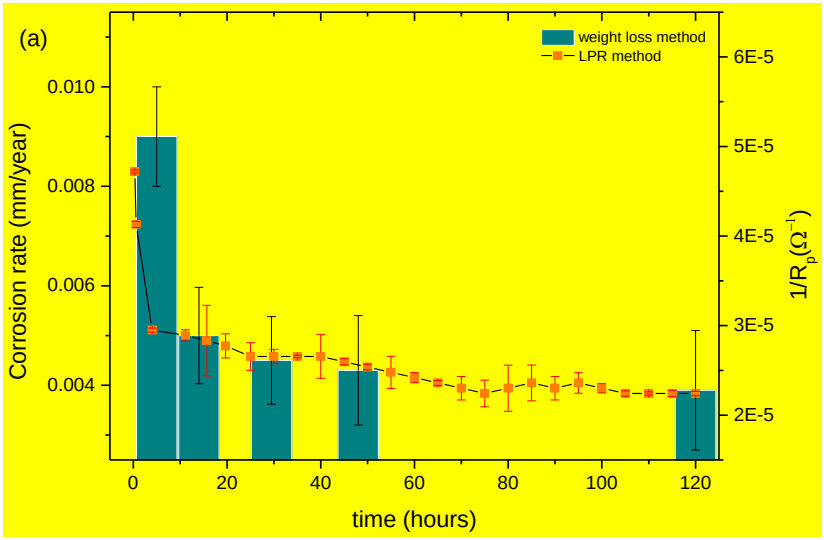


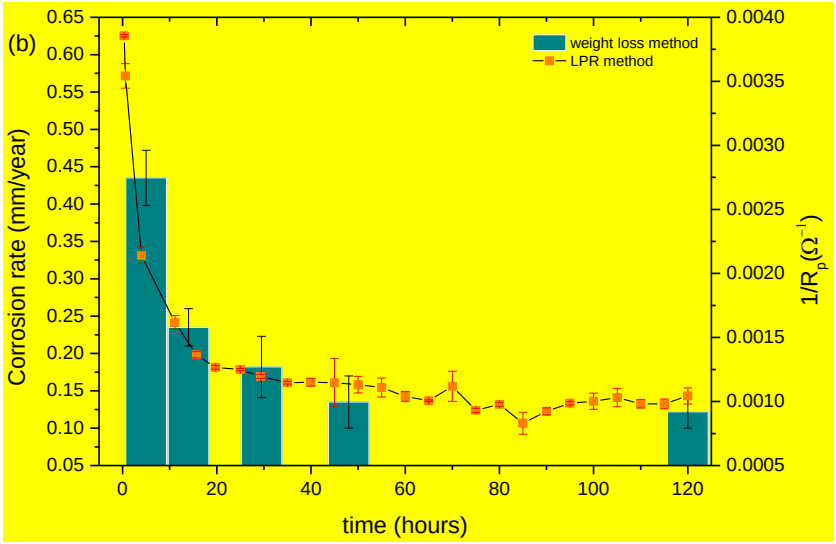

Figure 2. Corrosion rates and Rp of super 13Cr stainless steel with different immersion times at (a) 90°C and (b) 200°C.

***The passive film observed at 90°C***

Fig. 3 shows the macroscopic images for super 13Cr stainless steels before and after exposing to 90°C conditions at various immersion times, respectively. All the samples look the same as before testing and no corrosion products were observed on the surfaces. Referring to Fig. 2a, low corrosion rates of 0.04 mm/year were observed for super 13Cr at 90°C. The results suggest that super 13Cr could obviously keep in the primary passive state without any further corrosion at this test condition.

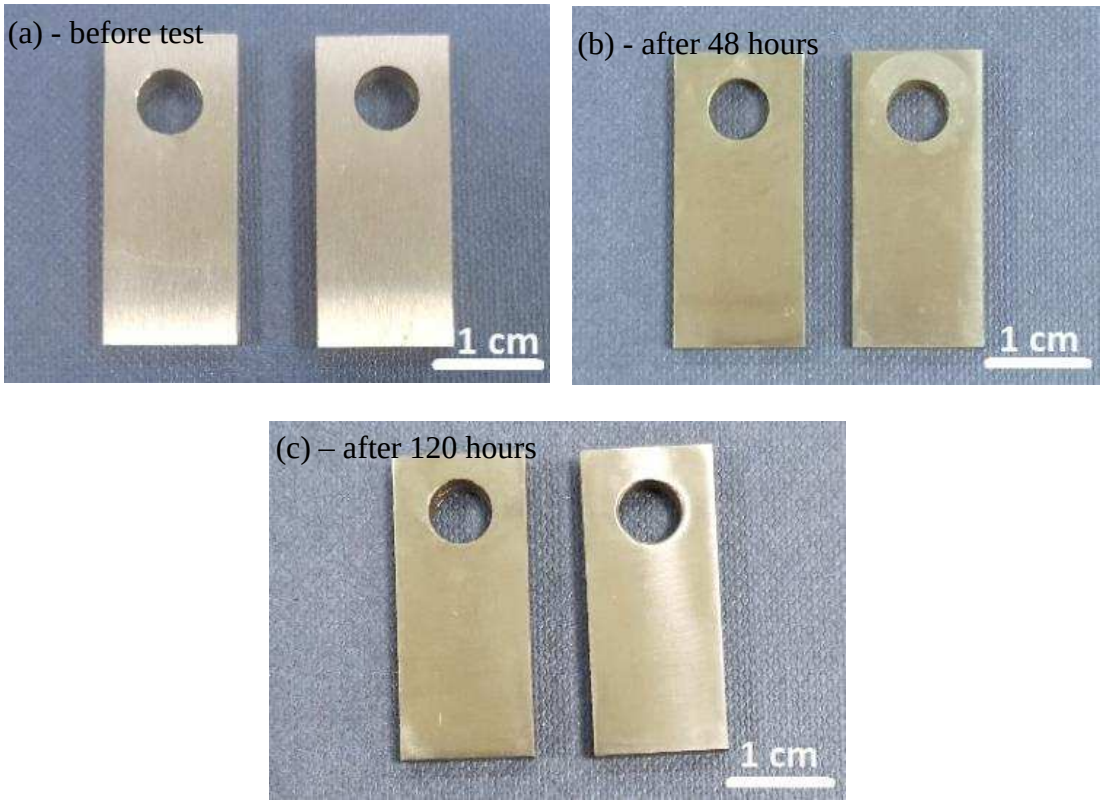


Figure 3. Macroscopic morphology of super 13Cr in 90°C condition at different immersion times (a) before test, (b) 48 h and (c) 120 h.

In order to observe the presence of the passive film on the super 13Cr surface after exposing to $CO_2$-saturated 4.86 wt. % NaCl solution after 5 days at 90°C, the milled FIB sample was mounted on a copper net for further TEM analysis. The high-angle annular-dark-field (HAADF) mode and EDS (Energy Dispersive X-Ray Spectroscopy) analysis were performed and the results are shown in Fig. 4. The results indicate the presence of a dense and compact passive

film at 90°C. The thickness of the film is approximately 20 nm and uniformly distributed on the entire super 13Cr surface. EDS mapping analysis indicates the enrichment of Cr and O in the film and similar elemental content within the passive film has been reported in a previous study [33]. Cross-sectional high-resolution transmission electron microscopy (HRTEM) images (Fig. 4b) of the sample showed no lattice fringes in the passive film which indicates the film formed at 90°C is an amorphous layer in nature. To characterize the composition of the passive film, high-resolution XPS was employed, the results are shown in Fig. 4d. The fitting curves of the peak binding energies indicate that Cr is present in the state as $Cr_2O_3$ and $Cr(OH)_3$ at 576.7 eV and 577.3 eV, respectively [34]. Thus, it can be speculated that the passive films are mainly composed of chromium-oxides and chromium-hydroxides. Similar observations were reported by Zhang et al. [9], which indicated the layer is mainly comprised of $Cr_2O_3$ with small amounts of $Cr(OH)_3$.

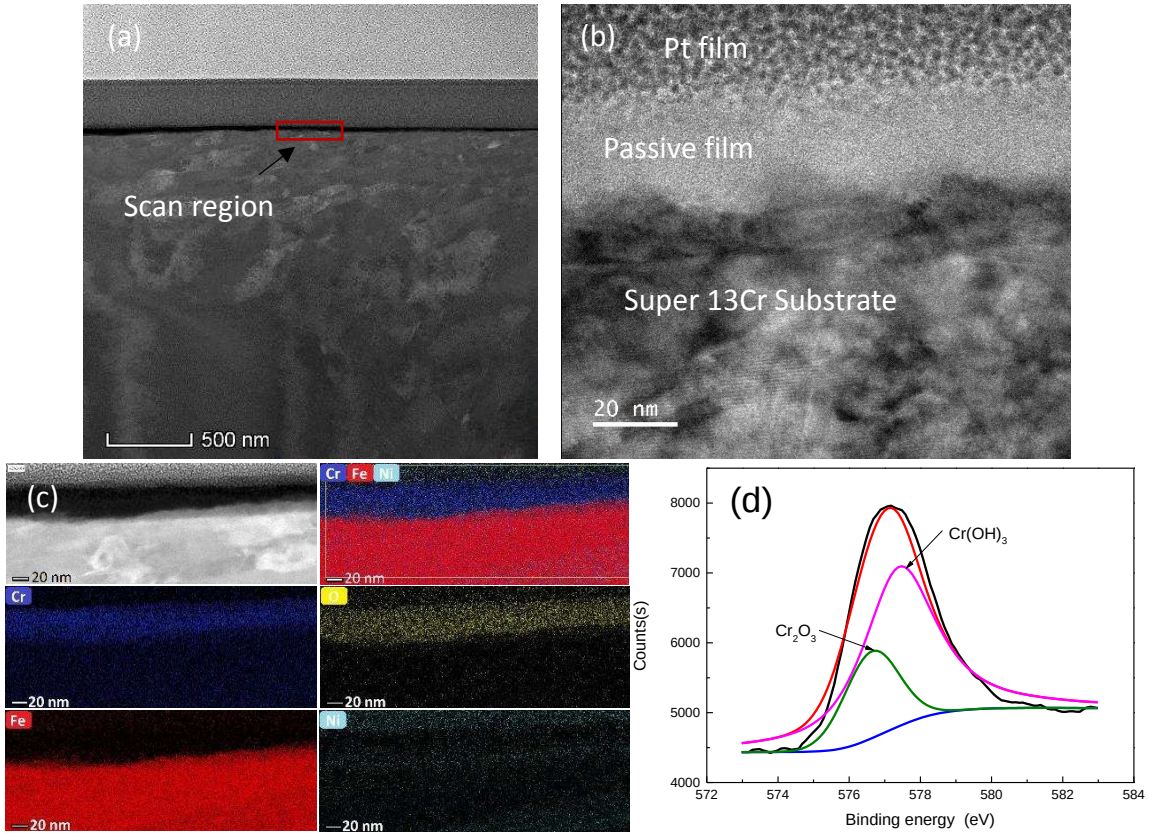


Figure 4. (a) TEM image of the passive film formed in 90°C condition, (b) HRTEM image of the film and (c) increased the magnification of the passive film cross-section, showing TEM-based EDS mapping, (d) XPS spectra of Cr 2p3/2 peaks.

***The effect of time on the formation of corrosion product films at 200°C***

Fig. 5 provides the top-view and cross-section SEM images of super 13Cr stainless steel exposed to $CO_2$-saturated 4.86 wt. % NaCl at 200°C and $CO_2$ partial pressure of 2.8 bar at different immersion times. The SEM images of the super 13Cr stainless steel surface indicate different surface morphologies for samples exposed to 200°C compared to that of 90°C. As shown in Fig. 5a and 5b, no obvious corrosion product exists and the polishing marks are clearly visible on the surface.

After 14 h of exposure, some scattered crystal grains were found on the surface (Fig. 5c and 5d) and increased in number with immersion time up to 29.5 hours as shown in Fig. 5e and 5f. It is interesting to note that the polishing marks are shallow, which might correspond to the formation of another layer that the large crystals precipitate on. However, the cross-sectional SEM images indicate that this inner layer is too thin and SEM cannot detect it. After 48 hours, the crystals appeared on the entire surface as shown in Fig. 5g and 5h. Referring to Fig. 2b, the reduction in corrosion rate suggests that another layer exists on the super 13Cr surface but at the nm scale. More details on analyzing the film evolution are given in the later sections.

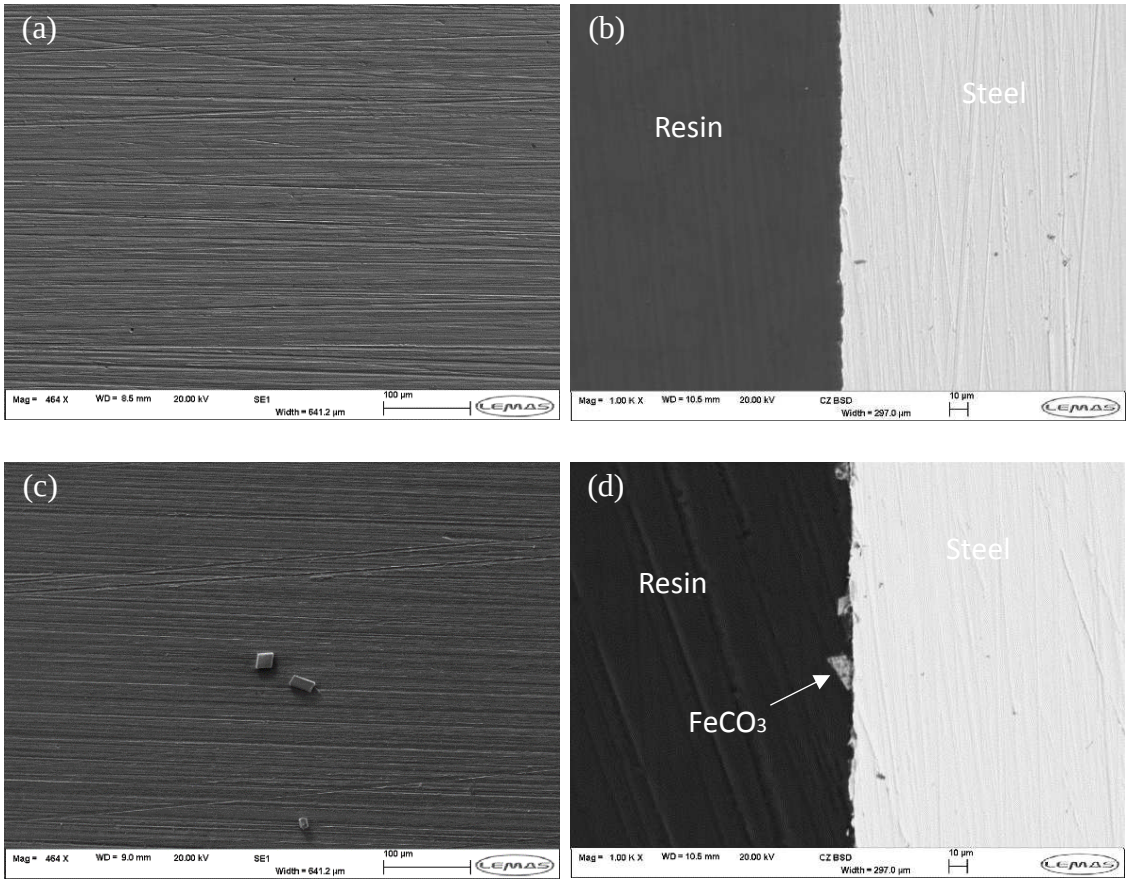

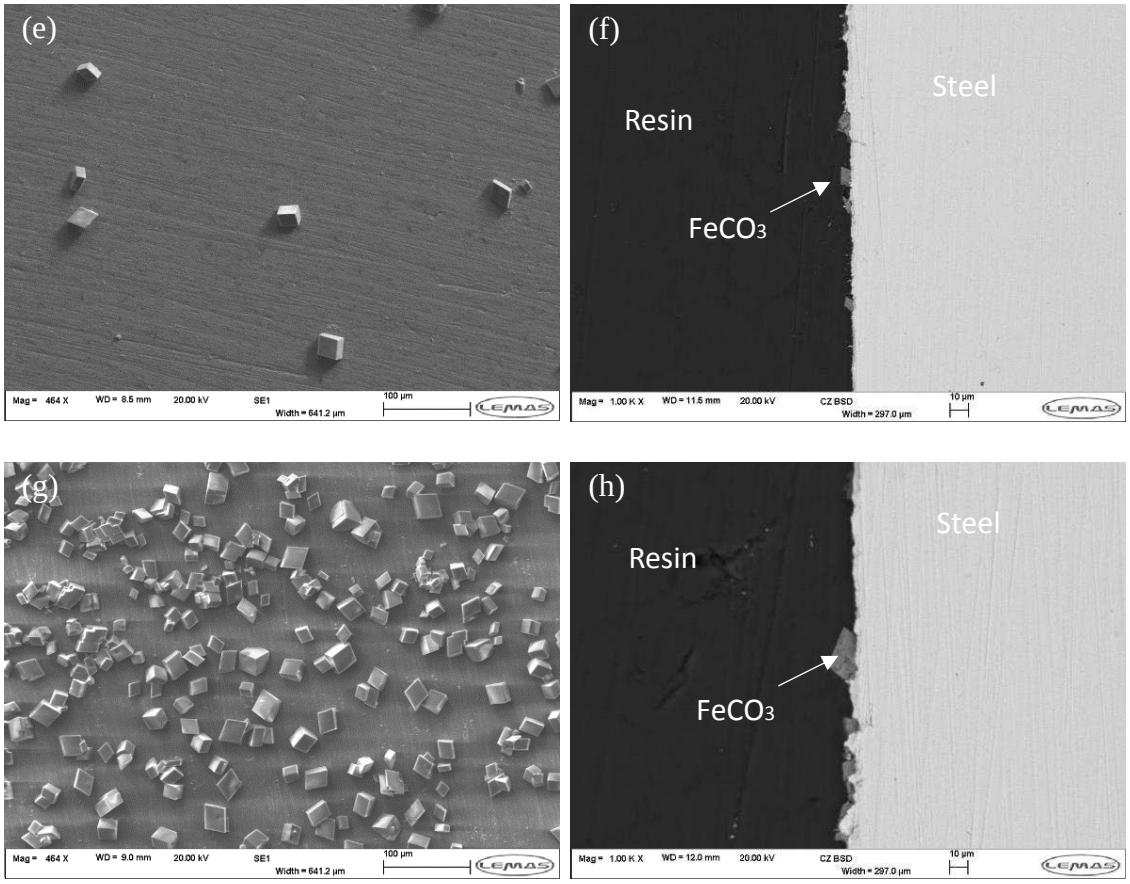


Figure 5. SEM surface (SEI, BSD) and cross-sectional morphology of the corrosion scale (a) and (b) 5h, (c) and (d)14h, (e) and (f) 29.5h, and (g) and (h) 48h.

After 120 h, the size of the crystals increased significantly, but the number of crystals was reduced as shown in Fig. 6. The cross-sectional morphology as shown in Fig. 6b indicates that the corrosion product layers formed on super 13Cr stainless steel are double layer structures, comprising an inner and outer layer. It is interesting to note that the thickness of the inner layer was not uniformly distributed, and ranged between 0.1μm and 4μm across the entire surface. In order to identify the corrosion product composition, XRD was utilized.

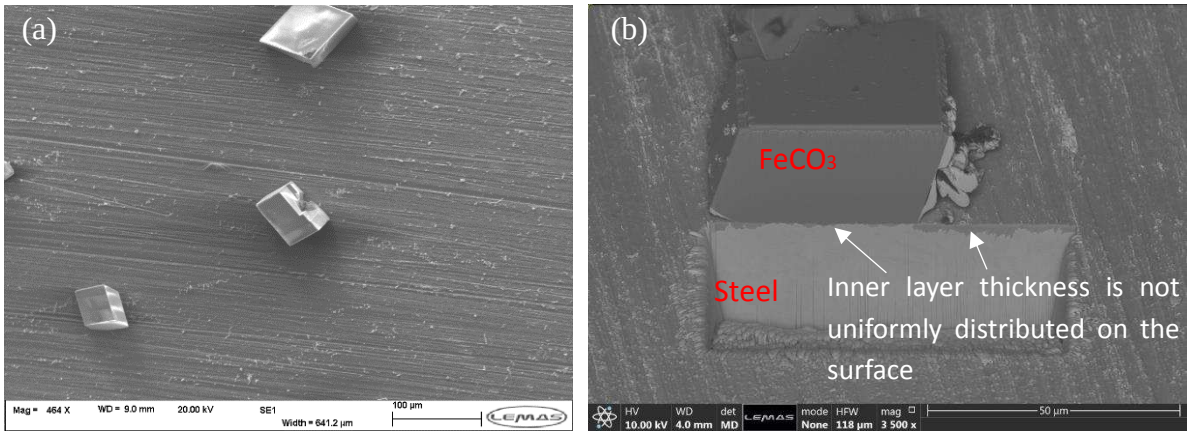


Figure 6. (a) Top-view SEM and (b) Fibs cross-section morphology of the corrosion scale after 120h exposure time.

Fig.7 illustrated the X-ray diffraction patterns of the corrosion product films formed on super 13Cr surface at various immersion times. The corrosion products were confirmed as $FeCO_3$ for samples exposed to 5h, 14h, 30h, and 48 hours. As increasing the immersion time from 5 hours to 14 hours, the $FeCO_3$ peaks become clear. However, the corrosion products are mainly comprised of $FeCO_3$ and $FeCr_2O_4$ for samples exposed for 120 hours. It is interesting to note that no $FeCr_2O_4$ crystals were observed for shorter immersion times by XRD measurements and suggests that this layer might be too thin and XRD cannot detect it. Therefore, the localized Raman spectroscopy at specific locations on the steel surface was used to supplement XRD measurements for super 13Cr exposed to shorter experiments.

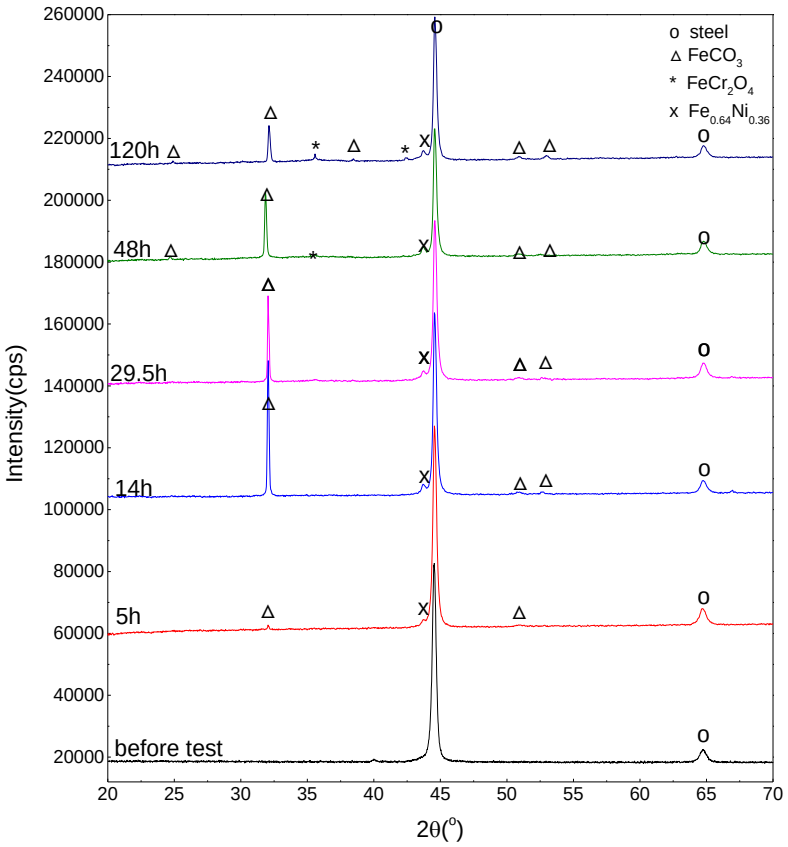


Figure 7. XRD patterns of super 13Cr specimens exposed at 200 °C for 5, 14, 29.5, 48 and 120h.

The Raman spectra provided in Fig. 8 relate to four scans conducted on super 13Cr surface at various immersion times. The spectra provided in Fig. 8a and 8b relate to two scans conducted on the sample exposed to 200°C after 120 hours; one on a large crystal as shown in Region A and one on an adjacent location in Region B. The spectra from Region A indicated the strong Raman peaks observed at 283 $cm^{-1}$ and 1085 $cm^{-1}$ and small peak at 735 $cm^{-1}$ over the crystals are representative of $FeCO_3$ and scans in Region B indicated the peaks corresponding to the $FeCr_2O_4$ are located at 555 $cm^{-1}$ and 695 $cm^{-1}$.

Fig. 8c and 8d indicated the main peak located at 695 $cm^{-1}$ which corresponds to the inner layer confirmed as the presence of $FeCr_2O_4$. These observations suggest that the inner layer of $FeCr_2O_4$ is present across the entire stainless steel surface, which must be responsible for the high corrosion resistance under these conditions.

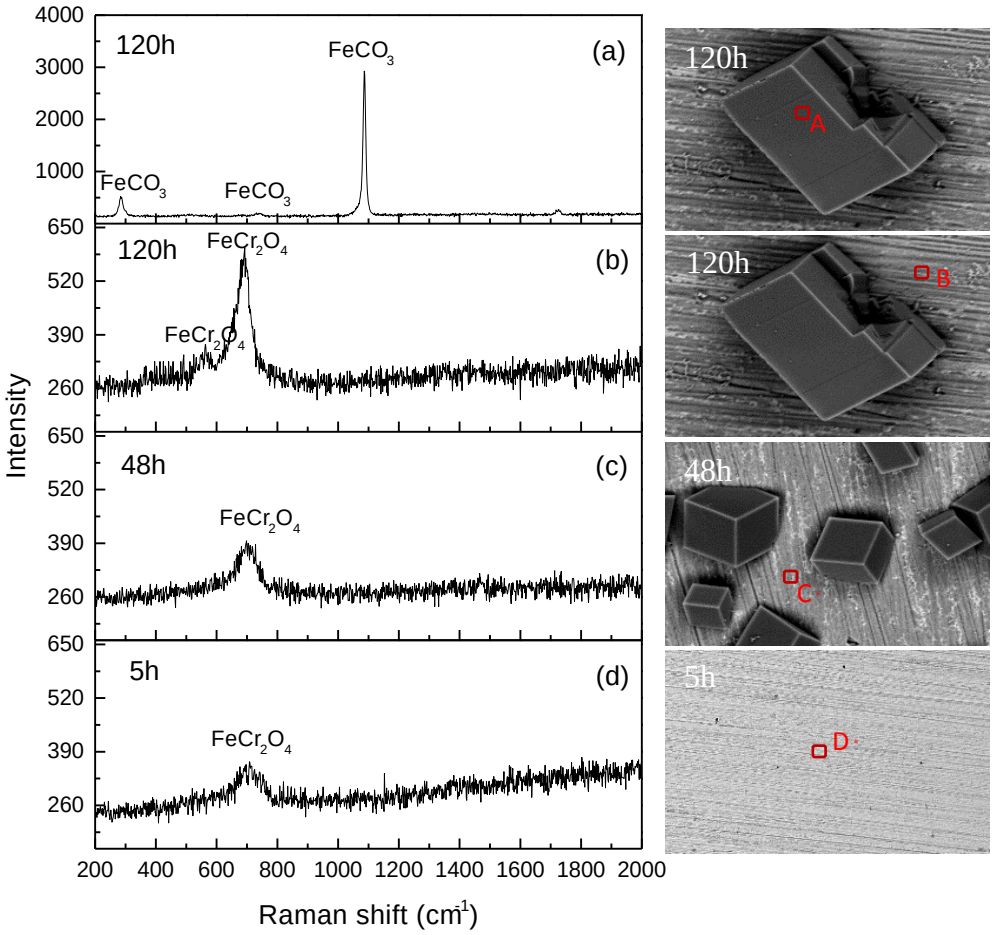


Figure 8. Raman spectra of super 13Cr specimens exposed to formation water at 200 °C for 5 h, 48 h, and 120h.

The XPS results in Fig. 9 indicate the composition of corrosion product films by specifying the sputtering time. The Fe 2p3/2 and Cr 2p3/2 peaks for super 13Cr indicate a different composition of corrosion products at 200°C compared to that of forming at 90°C. The fitting curve of the Fe 2p3/2 peak confirm the peaks at 709 eV, 710.3 eV and 713.8 eV are $FeCr_2O_4$ and the peaks are located at 712 eV and 715.6 eV corresponding to $FeCO_3$ [34]. Meanwhile, peaks of $Cr_2O_3$ and $Cr(OH)_3$ along with $FeCr_2O_4$ are separated and fitted well with the measured Cr spectra [34,35]. Therefore, the development of the corrosion product films detected on the surface of super 13Cr at 200°C is mainly $FeCr_2O_4$, $FeCO_3$, $Cr(OH)_3$ and $Cr_2O_3$.

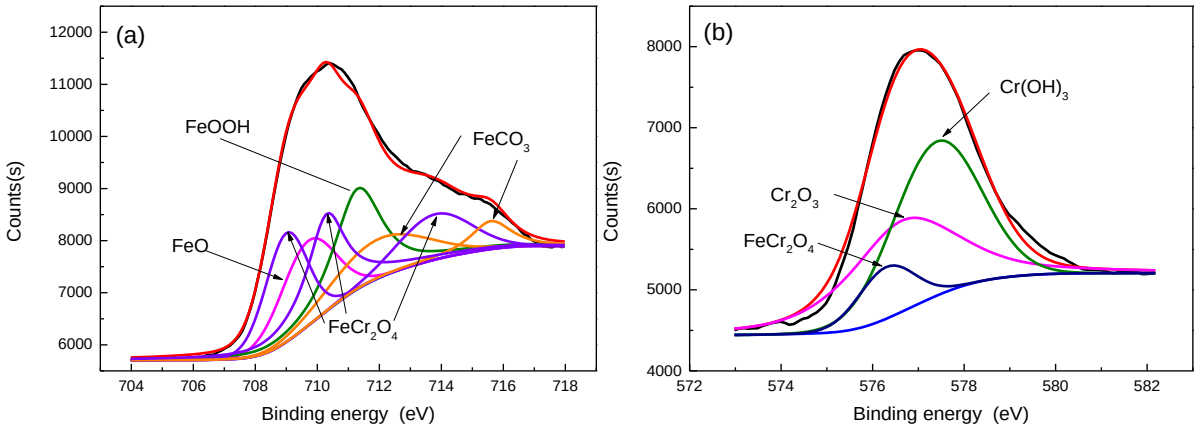


Figure 9. XPS spectra of the passive film formed at 200 °C condition, (a) Fe 2p3/2 peaks, (b) Cr 2p3/2 peaks.

***Further analysis of the formation of $FeCO_3$ and $FeCr_2O_4$ at 200°C***

To further understand the characteristics of the film developed on the surface of super 13Cr at 200°C, and distinguish the essential differences to the film formed on the surface at 90°C, a combination of FIB-SEM and TEM was employed. The sample exposed to $CO_2$-saturated 4.86%NaCl solution at 200°C for 120 h was selected and taken for further analyses of its composition and morphology. Fig. 10a shows the SEM images of a selected area of the corrosion product film at 200°C. A sample (Fig. 10b) was cut from this area and then ion milled to 100nm thick (Fig. 10c). The size of the large individual crystals on the sample surface exposed to 4.86 wt.% NaCl reached approximately 5-20 µm after 120 h exposure. Most importantly, the corrosion product displays a double-layered structure comprising an inner $FeCr_2O_4$ and outer $FeCO_3$ layer. The thickness of the inner corrosion product layer at 200°C is non-uniform and is varied between 0.5 and 3µm after 120 hours of exposure.

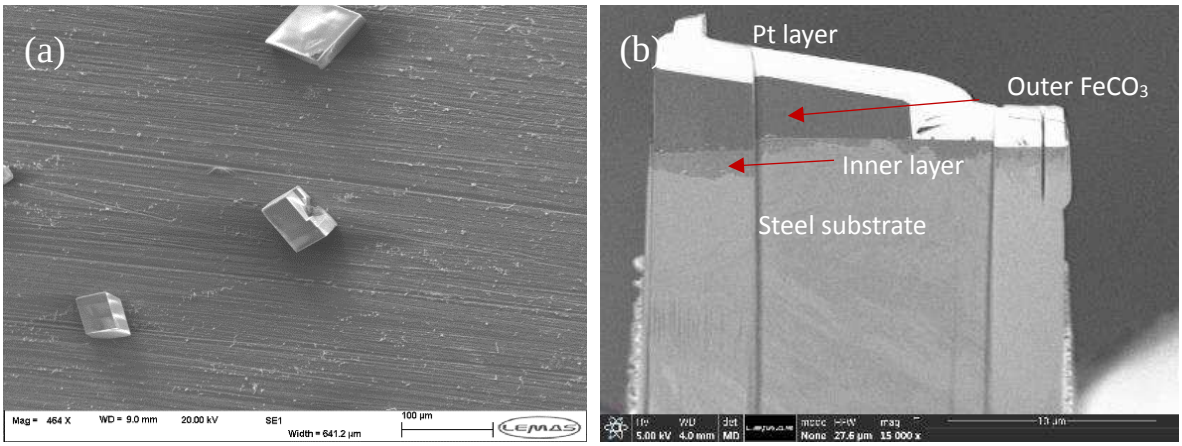


Figure 10. SEM images of analysis region (200°C sample) after 120 h, indicating (a) where ion

milling was performed on the sample surface prior to Pt deposition, (b) the sections milled away within the surface to produce the TEM sample

Fig. 11 presents the TEM analysis of the sample exposed to the $CO_2$-saturated 4.86%NaCl solution at 200°C and 2.7 bar of $CO_2$ partial pressure for 120 hours. The electron diffraction pattern indicates that the outer layers are confirmed as $FeCO_3$ crystals (Fig. 11b), the most important thin non-uniformed inner layer observed under the $FeCO_3$ crystals as shown in Fig. 11c is confirmed as nano-polycrystalline $FeCr_2O_4$.

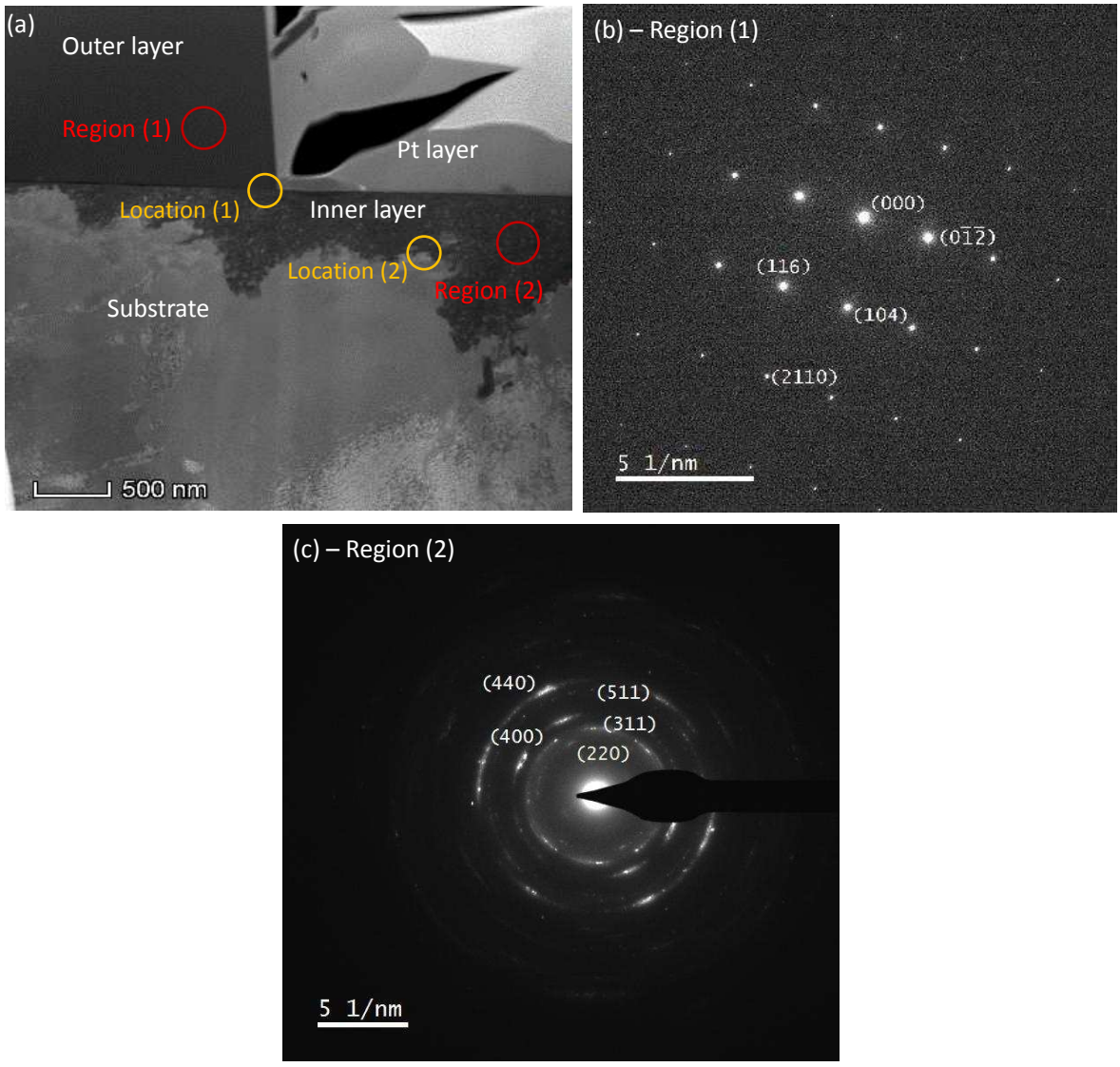


Figure 11. (a) TEM image of the passive film formed in 200°C condition, (b) the electron diffraction pattern corresponding to Region (1), (c) the electron diffraction pattern corresponding to Region (2).

TEM-EDS mapping analysis was used to further study on the interlayer between the crystalline $FeCO_3$ and the nano-polycrystalline $FeCr_2O_4$ layer as shown in Fig. 12. The TEM-EDS mapping

analysis (Figs. 12c) indicates a separated thin layer with approximately 20 nm was observed underneath the crystalline $FeCO_3$. The high concentration of Cr, Fe, and O with small amounts of Ni can be observed from the thin layer. Considering the sputtering depth (removal of 10 nm thickness), the results obtained by XPS indicated the thin corrosion product layer is mainly comprised of $Cr_2O_3$ and $Cr(OH)_3$.

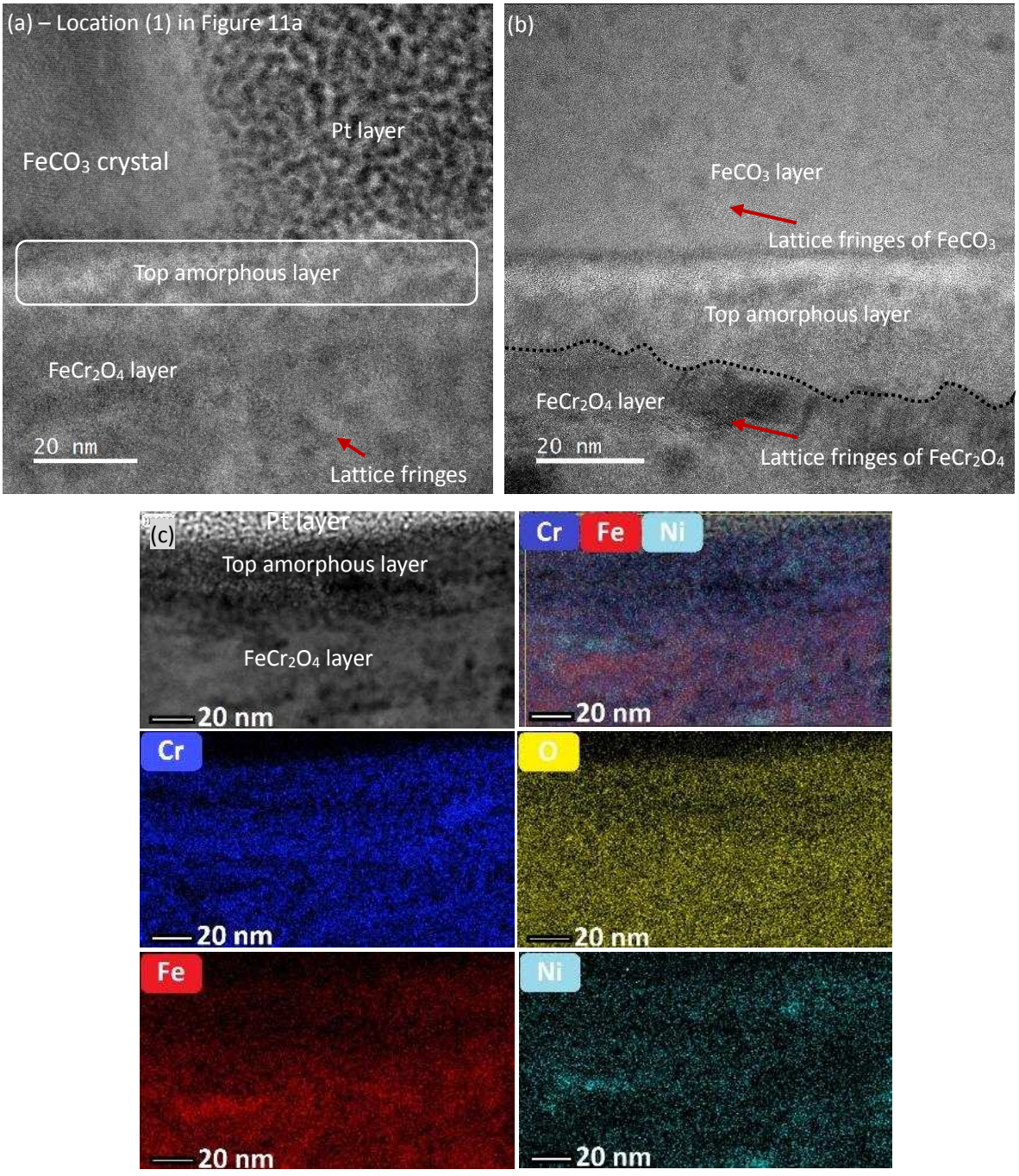


Figure 12. (a) HRTEM image on Location (1) in Fig. 10a, (b) HRTEM image beneath $FeCO_3$ crystal, and (c) Super-X EDS mapping of the outer interface

For the inner interface between nano-polycrystalline $FeCr_2O_4$ and steel substrate, it could be noticed that significant nickel exists covering the steel matrix. Besides, the growth of the film to the matrix was not all connected, some isolated matrix islands free from corrosion are surrounded by a rich nickel layer, which suggests that the nickel rich layer may play an important role in the resistance from corrosion by blocking the material interface and act as a barrier to restrict the corrosive species pass through and reduce the material degradation. A similar observation was reported by Terachi et al. [36], that a nickel enrichment layer was observed at the oxide/metal interface for 316 stainless steel in simulated pressurized water reactors at 320°C. It can be suggested that the formation of the Ni-rich layer can provide preferential iron or chromium dissolution reactions on the material surface.

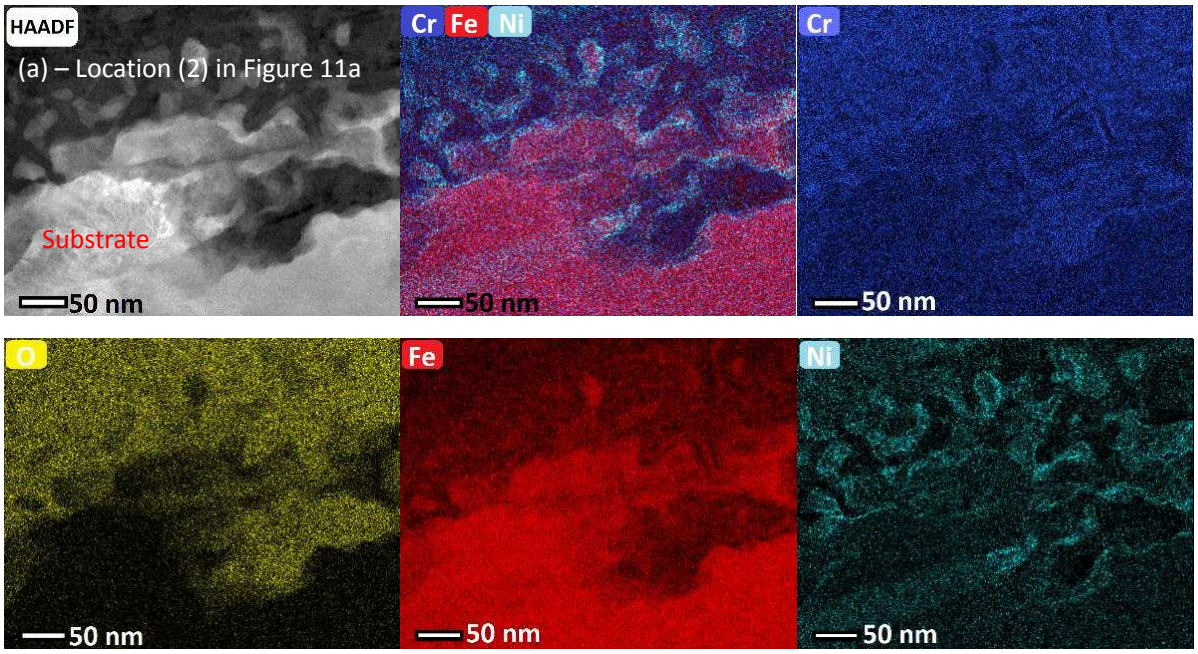


Figure 13. Super-X EDS mapping of the inner interface of film cross-section.

## *Discussion*

### *Effects of temperature and immersion time on thermodynamics*

To better understand the formation of the corrosion products on super 13Cr exposed to $CO_2$-saturated solution at 90°C and 200°C, Pourbaix diagrams are used to identify the thermodynamically-stable corrosion products formed on the surface as the temperature is increased.

It is known that super 13Cr has low corrosion sensitivity at 90°C, in which $10^{-8}$ mol/L can be

used for the concentrations of total dissolved metal cations [37]. However, for samples exposed to 200°C as referred to in Fig. 2b, super 13Cr becomes more sensitive as increasing in temperature and high corrosion rates of 0.45 mm/year were recorded. The total metal cation concentration of $10^{-5}$ mol/L was used. A similar value of $10^{-6}$ mol/L was reported by Zhao et al. [19], who conducted the Pourbaix diagrams for super 13Cr at a lower temperature (90 °C - 180°C) after a long immersion time of 30 days. The thermodynamic data are used to generate the diagrams as provided in supplementary document in Table S1

Referring to the literature for an in-situ pH measurement on 316L stainless steel, it is well known that the pH of the bulk solution remained almost unchanged when the material is in the passive state, while the pH value at the material interface increases after prolonged immersion time [38]. Fig. 14 shows the Pourbaix diagrams for 90°C condition and $CO_2$ partial pressure of 1.3 bar for Fe-Cr-$Cl^-$-$CO_2$-$H_2O$ system. The measured OCP potential as shown in Fig. 2a was in the passive ranges of -0.38 – -0.365 V vs SHE at 90°C, and the calculated solution pH was 6.01 (Table. 2). Considering the region as shown in Fig. 14, it is clear that the formation of $Cr_2O_3$ and $Cr(OH)_3$ can be observed on the surface indicating the passive state of super 13Cr for Fe-Cr-$Cl^-$-$CO_2$-$H_2O$ systems. The hydroxide $Cr(OH)_3$ and $Cr_2O_3$ form via the following reactions [19,39]:

$$2Cr(OH)_3 \leftrightarrow Cr_2O_3 + 3H_2O \quad (7)$$

$$2Cr + 3H_2O \leftrightarrow Cr_2O_3 + 6H^+ + 6e^- \quad (8)$$

$$Cr + 3H_2O \leftrightarrow Cr(OH)_3 + 3H^+ + 3e^- \quad (9)$$

Both experimental results and constructed Pourbaix diagram suggest that the passive film at the pH of 6 is mainly comprised of $Cr_2O_3$ and $Cr(OH)_3$ for sample exposed to 90°C which enhances the material corrosion resistance.

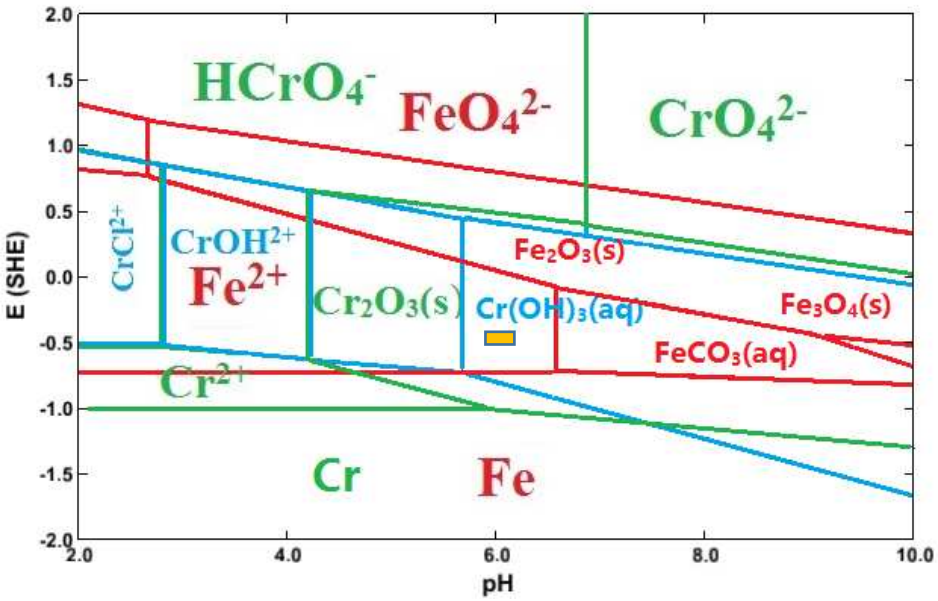


Figure 14. Pourbaix diagrams for Fe-Cr-$Cl^-$-$CO_2$-$H_2O$ system at 90°C with the concentration level of $10^{-8}$ mol/L for dissolved metal cations. The thermodynamically stable corrosion products in the test condition are marked within the orange area.

Fig. 15 indicates the constructed Pourbaix diagrams at 200°C and $CO_2$ partial pressure of 2.7 bar for Fe-Cr-$Cl^-$-$CO_2$-$H_2O$ system. For super 13Cr exposed to 200°C, the measured OCP potential was in the range of -0.625 – -0.64 V vs SHE as shown in Fig. 2b, and the calculated solution pH value by using OLI was 6.41. Refer to the literature, the surface pH can be higher (not to exceed 6.9) than that of the bulk solution [21]. The thermodynamic results suggest that the stable corrosion products at pH ranges between 6.41 and 6.9 are mainly comprised of $FeCr_2O_4$, $Cr(OH)_3$ and $FeCO_3$.

It is clear that the interaction between Fe and Cr can result in the formation of oxide $FeCr_2O_4$ on super 13Cr surface. In view of the TEM images and the electron diffraction pattern as shown in Fig. 10, it is clear that the formation of corrosion product film is mainly $FeCr_2O_4$, and the precipitates on the surface also contain $FeCO_3$ (the large cubic crystals as shown in Fig. 5). Observation of $Cr(OH)_3$ has been reported by Yue et al. [16], who worked with super 13Cr in $CO_2$-saturated water at temperature ranges of 120°C and 150°C. We reported that the amorphous $Cr(OH)_3$ can be detected by using XPS at the surface, agreeing with the observations here. Zhao et al. [20], concluded similar results by using the TEM and XPS analysis to identify the amorphous $Cr(OH)_3$ layer. The Pourbaix diagrams as shown in Fig. 14 and 15 indicate that as the temperature increases from 90 to 200°C, $FeCr_2O_4$ becomes one of

the thermodynamically more favorable corrosion products. Increasing temperature from 90°C to 200°C extends the $Cr_2O_3$ region to a lower pH range. It is these shifts which results in the transition from $Cr_2O_3$ to $FeCr_2O_4$ with increasing temperature.

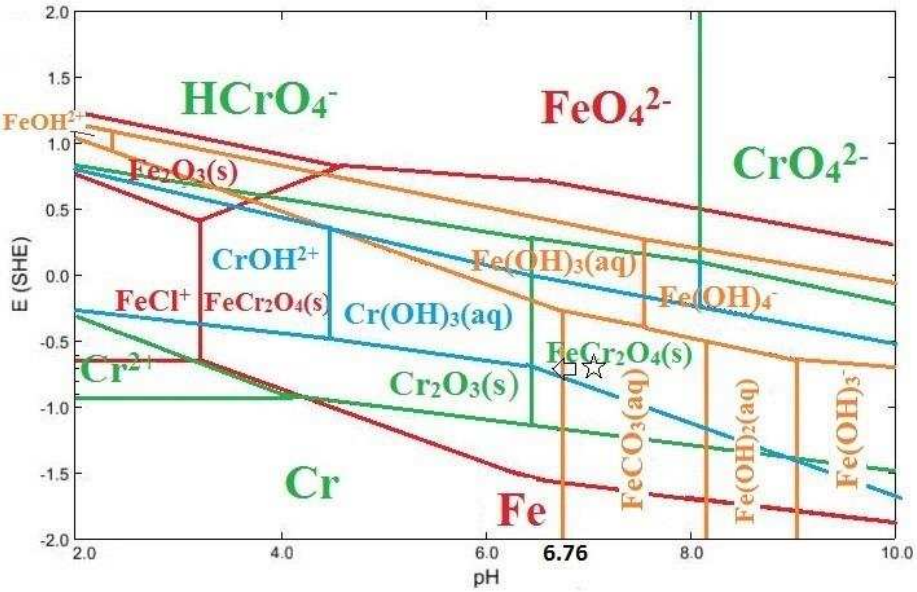


Figure 15. Pourbaix diagrams for Fe-Cr-$Cl^-$-$CO_2$-$H_2O$ system at 200°C with the total metal cations concentration level of $10^{-5}$ mol/L.

***Corrosion product film evolution mechanism at 200°C***

***Supersaturation, nucleation and crystal growth of the outer $FeCO_3$ crystals***

Refering to Fig. 5 and Fig. 6, it is clear that the formation of $FeCO_3$ in term of crystal size and number can be related to $FeCO_3$ supersaturation, the nucleation, and particle growth rates. In principle, crystallization results from these three processes which interact mutually: supersaturation, nucleation and crystal growth. The nucleation of $FeCO_3$ is initiated on the surface once supersaturated (*SR*) with respect to $FeCO_3$ is reached:

$$SR = \frac{[Fe^{2+}][CO_3^{2-}]}{K_{SP}} \quad (10)$$

where *SR* is the supersaturation of $FeCO_3$, $K_{sp}$ is the solubility product for $FeCO_3$ in $mol^2/L^2$, $[Fe^{2+}]$ is the concentration of $Fe^{2+}$, and $[CO_3^{2-}]$ is the concentration of $CO_3^{2-}$ [40].

The formation of $FeCO_3$ on the surface when a specific value of the supersaturation is being exceeded e.g. SR> 1. As the prolonged immersion time is pologed, the concentration of $Fe^{2+}$ and $CO_3^{2-}$ significantly exceeds the solubility of $FeCO_3$ due to the relative high corrosion rate, a higher supersaturation will be obtained. Previous research proved that the rate of nucleation

increases exponentially with relative supersaturation, whereas the rate of particle growth increases linearly with relative supersaturation [41]. As a result, the nucleation rate far exceeds the particle growth rate, thereby preventing particle growth from happening and leading to the $FeCO_3$ crystals only increasing in number within 48 hours. A similar observation was reported by Gao et al. [41].

After 120 hours, a lower corrosion rate indicated that $Fe^{2+}$ dissolution decreased to a stable level, results in the concentration of $[Fe^{2+}][CO_3^{2-}]$ decreased. It is known that the nucleation rate of $FeCO_3$ falls exponentially with saturation value, whilst particle growth decreases in a linear fashion [23]. Consequently, particle growth is believed to dominate for longer immersion test as large cubic $FeCO_3$ can be observed on the surface as shown in Fig. 6a. Research has shown that in the case of precipitation reactions at low relative supersaturation, the process is believed to be dominated by crystal growth [42].

***The formation of $Cr_2O_3$ and $FeCr_2O_4$ on the surface***

T pourbaix diagram at 200°C shows that the formation of a thin $FeCr_2O_4$ layer was via Reaction (11) – (13) (noting that all these reactions produce $H^+$ ions, potentially acidifying the interface during formation) [19,39]:

$$Fe + 2Cr + 4H_2O \leftrightarrow FeCr_2O_4 + 8H^+ + 8e^- \quad (11)$$

$$Fe^{2+} + Cr_2O_3 + H_2O \leftrightarrow FeCr_2O_4 + 2H^+ \quad (12)$$

$$Fe^{2+} + 2Cr(OH)_3(aq) \leftrightarrow FeCr_2O_4 + 2H^+ + 2H_2O \quad (13)$$

Meanwhile, a large amount of hydroxide $Cr(OH)_3$ forms via Reaction (9) in the aqueous phase due to high corrosion rate (approx. 0.43mm/year) for the first 5 hours. Therefore, the local surface pH will be decreased due to reactions (8 - 13) which produced $H^+$ ions on the surface [23]. In the discussion of thermodynamics, the formation of $Cr_2O_3$ is not well explained. Small amounts of $Cr_2O_3$ form on the surface via Reactions (8 and 9) once the surface pH decreased to 6.32 according to Pourbaix diagram as shown in Fig. 15. In addition, the presence of $Cr_2O_3$ may also result from the residual pre-existing passive film damaged at high temperature.

In view of the HRTEM images in Fig. 12c suggested a nanoscale amorphous layer of 20nm in thickness was observed at the interface between crystal $FeCO_3$ and $FeCr_2O_4$. The use of TEM suggests that it mainly comprised $Cr_2O_3$ and supposed to be locally generated in acidification

at the material interface. The enrichment of Cr and Ni can be observed randomly distributed within this film compared to the compositions of the passive film as shown in Fig. 4, which cause the limitation to resist high temperature corrosion.

***The formation of $FeCr_2O_4$ and a nickel enriched inner interface***

It can be seen that the main difference in the corrosion resistance of super 13Cr at 200°C and temperature below 90°C is the performance variation between corrosion product film and the presence of a passive film. First of all, the composition changing from $Cr_2O_3$ to $FeCr_2O_4$ contributed to the material deterioration. It was found that the chromium ions are tightly bounds with neighbors in the spinel structure compared to iron cations at low temperature [21,43]. The $Cr^{3+}$ sites occupied by $Fe^{2+}$ in the spinel structure are able to damage the passive film protectiveness. Besides, for high temperature corrosion processes, the generation of $FeCr_2O_4$ provides more pathways as shown in Fig.16, leading to a large driving force for cation transport through the inner interface. On the contrary, the $Cr^{3+}$ sites contained in $FeCr_2O_4$ decrease the number of available vacancy diffusion paths [43], thereby slowing down the corrosion via the growth of the chromium enriched film [44].

In addition to the blocking effect of chromium on available vacancy diffusion paths, the nonreactive nickel covering the matrix occupied a large amount of vacancies on the inner interface (Fig. 17), effectively preventing the formation and transfer/transport of iron ions. Fig. 16 presents the line scan from the deposited corrosion product to matrix, showing obvious Ni enrichment in every interface in the film. The results suggest that the Ni enrichment layer at the material interface plays a critical factor in the kinetics of the transformation of the film that requires the consumption of $Cr^{3+}$ and $Fe^{2+}$. The faster kinetics of coalescence and crystallization can be favored by the slower rate of production of $FeCr_2O_4$. The rate of production of $FeCr_2O_4$ is lower than the rate of crystallization so that a more advanced crystallization of $FeCr_2O_4$ can be achieved after a given period of time. Thus, the Ni enrichment within the films limits the dissolution rate at which Cr and Fe become available for the formation of $FeCr_2O_4$, leading to a nanocrystalline film (confirmed in Fig. 10), results in decreasing in corrosion rate.

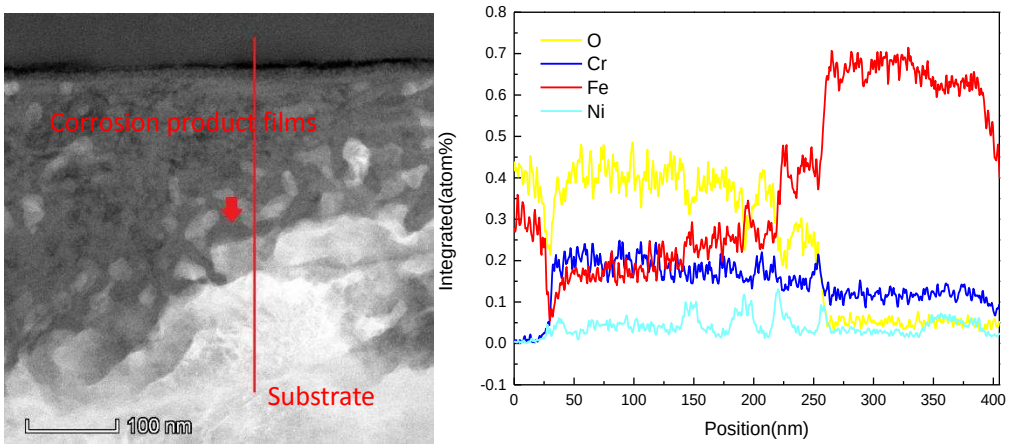


Figure 16. Line scan of the film cross-section of super 13Cr in 200°C condition.

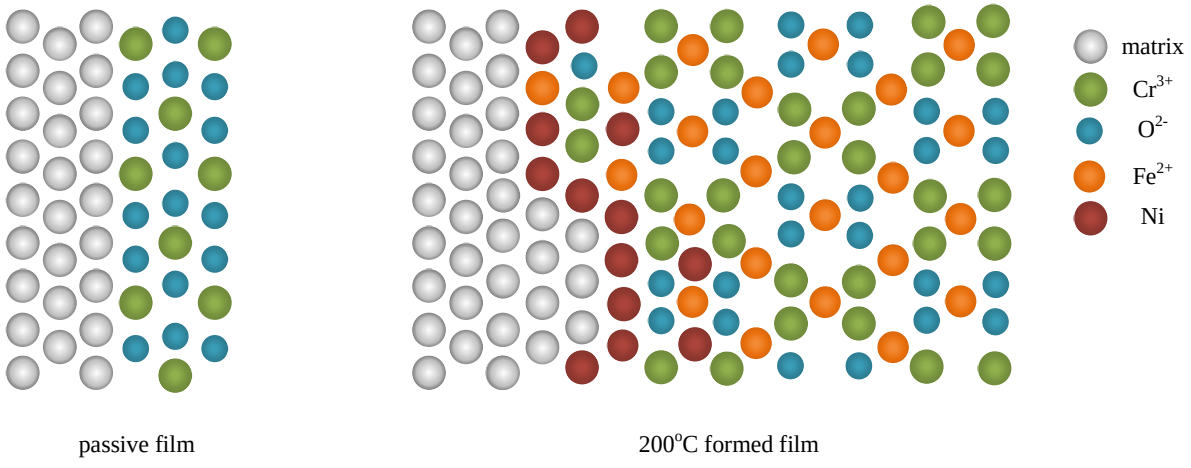


Figure 17. The formation and transport of defects within the inner interface on super 13Cr at 200°C.

## *Conclusions*

The characteristics of corrosion product film and corrosion behaviour of super 13Cr stainless steel in a $CO_2$-saturated 4.86 wt.% NaCl solution has been compared at temperature of 90°C and 200°C respectively in this study, the study focused on the formation of corrosion product films on the surface at 200°C was compared with the typical passive film formed on the surface at 90°C. The following main conclusions can be made:

1. The formation of corrosion product films on super 13Cr at 200°C including three stages: Stage I, the replacement of the primary passive film to $FeCr_2O_4$; Stage II, the growth of the $FeCr_2O_4$-dominated phase in the layer and nucleation of crystalline $FeCO_3$; Stage III, thickening of the $FeCr_2O_4$ formed film and growth of crystalline $FeCO_3$.
2. The passive film formed at 90°C is an amorphous-like structure, mainly containing

$Cr_2O_3$. However, at 200°C, the nanoscale passive film was replaced by a microscale nanocrystalline $FeCr_2O_4$ confirmed by using Raman/TEM analysis.

3. The thickness of the passive film at 90°C is 20nm and uniformly distributed on the entire surface. The passive films are mainly comprised of $Cr_2O_3$ and $Cr(OH)_3$ which enhance the material corrosion resistance. The thickness of the inner corrosion product layer at 200°C is not uniform and is varied between 0.5 and 3μm after 120 hours of exposure.

4. A nickel rich layer plays an important role in the corrosion resistance at 200°C by blocking the material interface and act as a barrier to restrict the corrosive species pass through and reduce material degradation.

## *Reference*


[1] A.J. Sedriks, Corrosion of stainless steel, John Wiley and Sons, New York, 1979.

[2] L.T. Popoola, A.S. Grema, G.K. Latinwo, B. Gutti, A.S. Balogun, Corrosion problems during oil and gas production and its mitigation, Int. J. Ind. Chem. 4 (2013) 35.

[3] A. Turnbull, A. Griffiths, Corrosion and cracking of weldable 13 wt-% Cr martensitic stainless steels for application in the oil and gas industry, Corros. Eng. Sci. Technol. 38 (2003) 21–50.

[4] Y. Hua, R. Jonnalagadda, L. Zhang, A. Neville, R. Barker, Assessment of general and localized corrosion behavior of X65 and 13Cr steels in water-saturated supercritical CO2 environments with SO2/O2, Int. J. Greenh. Gas Control. 64 (2017) 126–136.

[5] K. Asami, K. Hashimoto, S. Shimodaira, An XPS study of the passivity of a series of iron—chromium alloys in sulphuric acid, Corros. Sci. 18 (1978) 151–160.

[6] S. Jin, A. Atrens, ESCA-Studies of the structure and composition of the passive film formed on stainless steels by various immersion temperatures in 0.1 M NaCl solution, Appl. Phys. A. 45 (1988) 83–91.

[7] R. Kirchheim, B. Heine, S. Hofmann, H. Hofsäss, Compositional changes of passive films due to different transport rates and preferential dissolution, Corros. Sci. 31 (1990) 573–578.

[8] C.-O. Olsson, D. Landolt, Passive films on stainless steels—chemistry, structure and growth, Electrochimica Acta. 48 (2003) 1093–1104.

[9] H. Zhang, Y. Zhao, Z. Jiang, Effects of temperature on the corrosion behavior of 13Cr martensitic stainless steel during exposure to CO2 and Cl- environment, Mater. Lett. 59 (2005) 3370–3374.

[10] J.-B. Lee, S.-W. Kim, Semiconducting properties of passive films formed on Fe–Cr alloys using capacitiance measurements and cyclic voltammetry techniques, Mater. Chem. Phys. 104 (2007) 98–104.

[11] K. Kondo, M. Ueda, K. Ogawa, H. Amaya, H. Hirata, H. Takabe, Y. Miyazaki, Alloy design of super 13 Cr martensitic stainless steel(development of super 13 Cr martensitic stainless

590 steel for line pipe-1), Supermartensitic Stainl. Steels99. (1999) 11–18.
591 [12] H. Amaya, T. Mori, K. Kondo, H. Hirata, M. Ueda, others, Effect of chromium and
592 molybedenum on corrosion resistance of super 13Cr martenistic stainless steel in CO2
593 environment, in: Corros. 98, NACE International, Paper No. 98113, 1998.
594 [13] M. Ueda, H. Amaya, K. Ogawa, K. Kondo, T. Mori, others, Corrosion resistance of weldable
595 super 13Cr stainless steel in H2S containing CO2 environments, in: Corros. 96, NACE
596 International, Paper No. 96058, 1996.
597 [14] W. Fredriksson, S. Malmgren, T. Gustafsson, M. Gorgoi, K. Edström, Full depth profile of
598 passive films on 316L stainless steel based on high resolution HAXPES in combination with
599 ARXPS, Appl. Surf. Sci. 258 (2012) 5790–5797.
600 [15] V. Maurice, W. Yang, P. Marcus, X-Ray Photoelectron Spectroscopy and Scanning
601 Tunneling Microscopy Study of Passive Films Formed on (100) Fe-18Cr-13Ni Single-Crystal
602 Surfaces, J. Electrochem. Soc. 145 (1998) 909–920.
603 [16] X. Yue, M. Zhao, L. Zhang, H. Zhang, D. Li, M. Lu, Correlation between electrochemical
604 properties and stress corrosion cracking of super 13Cr under an HTHP CO 2 environment,
605 RSC Adv. 8 (2018) 24679–24689.
606 [17] L. Mu, W. Zhao, Investigation on carbon dioxide corrosion behaviour of HP13Cr110
607 stainless steel in simulated stratum water, Corros. Sci. 52 (2010) 82–89.
608 [18] R. Moreira, C. Franco, C. Joia, S. Giordana, O. Mattos, The effects of temperature and
609 hydrodynamics on the CO2 corrosion of 13Cr and 13Cr5Ni2Mo stainless steels in the
610 presence of free acetic acid, Corros. Sci. 46 (2004) 2987–3003.
611 [19] Y. Zhao, J. Xie, G. Zeng, T. Zhang, D. Xu, F. Wang, Pourbaix diagram for HP-13Cr stainless
612 steel in the aggressive oilfield environment characterized by high temperature, high CO2
613 partial pressure and high salinity, Electrochimica Acta. 293 (2019) 116–127.
614 [20] Y. Zhao, X. Li, C. Zhang, T. Zhang, J. Xie, G. Zeng, D. Xu, F. Wang, Investigation of the
615 rotation speed on corrosion behavior of HP-13Cr stainless steel in the extremely
616 aggressive oilfield environment by using the rotating cage test, Corros. Sci. 145 (2018)
617 307–319.
618 [21] D.D. Macdonald, Passivity–the key to our metals-based civilization, Pure Appl. Chem. 71
619 (1999) 951–978.
620 [22] R. Barker, D. Burkle, T. Charpentier, H. Thompson, A. Neville, A review of iron carbonate
621 (FeCO3) formation in the oil and gas industry, Corros. Sci. 142 (2018) 312–341.
622 [23] S. Guo, L. Xu, L. Zhang, W. Chang, M. Lu, Corrosion of alloy steels containing 2% chromium
623 in CO2 environments, Corros. Sci. 63 (2012) 246–258.
624 [24] S. Guo, L. Xu, L. Zhang, W. Chang, M. Lu, Characterization of corrosion scale formed on
625 3Cr steel in CO2-saturated formation water, Corros. Sci. 110 (2016) 123–133.
626 [25] L. Zheng, J. Landon, N.S. Matin, K. Liu, FeCO3 coating process toward the corrosion
627 protection of carbon steel in a postcombustion CO2 capture system, Ind. Eng. Chem. Res.
628 55 (2016) 3939–3948.
629 [26] J. Heuer, J. Stubbins, An XPS characterization of FeCO3 films from CO2 corrosion, Corros.
630 Sci. 41 (1999) 1231–1243.
631 [27] OLI Systems, Inc., OLI Analyzer Studio, Vers.3.1, 108 American Road, Morris Plaines, New
632 Jersey, www.olisystems.com.
633 [28] P. Wang, A. Anderko, R.D. Young, A speciation-based model for mixed-solvent electrolyte

634 systems, Fluid Phase Equilibria. 203 (2002) 141–176.
635 [29] R.D. Springer, Z. Wang, A. Anderko, P. Wang, A.R. Felmy, A thermodynamic model for
636 predicting mineral reactivity in supercritical carbon dioxide: I. Phase behavior of carbon
637 dioxide–water–chloride salt systems across the H2O-rich to the CO2-rich regions, Chem.
638 Geol. 322 (2012) 151–171.
639 [30] R.D. Springer, P. Wang, A. Anderko, others, Modeling the Properties of H 2 S/CO
640 2/Salt/Water Systems in Wide Ranges of Temperature and Pressure, SPE J. 20 (2015)
641 1120–1134.
642 [31] ASTM G1-03 Standard Practice for preparing, cleaning, and evaluating corrosion test
643 specimens, ASTM Int'l 2011.
644 [32] D.D. Macdonald, A.C. Scott, P. Wentrcek, External reference electrodes for use in high
645 temperature aqueous systems, J. Electrochem. Soc. 126 (1979) 908–911.
646 [33] E. Hamada, K. Yamada, M. Nagoshi, N. Makiishi, K. Sato, T. Ishii, K. Fukuda, S. Ishikawa, T.
647 Ujiro, Direct imaging of native passive film on stainless steel by aberration corrected STEM,
648 Corros. Sci. 52 (2010) 3851–3854.
649 [34] M.C. Biesinger, B.P. Payne, A.P. Grosvenor, L.W. Lau, A.R. Gerson, R.S.C. Smart, Resolving
650 surface chemical states in XPS analysis of first row transition metals, oxides and
651 hydroxides: Cr, Mn, Fe, Co and Ni, Appl. Surf. Sci. 257 (2011) 2717–2730.
652 [35] M. Biesinger, C. Brown, J. Mycroft, R. Davidson, N. McIntyre, X-ray photoelectron
653 spectroscopy studies of chromium compounds, Surf. Interface Anal. Int. J. Devoted Dev.
654 Appl. Tech. Anal. Surf. Interfaces Thin Films. 36 (2004) 1550–1563.
655 [36] T. Terachi, K. Fujii, K. Arioka, Microstructural characterization of SCC crack tip and oxide
656 film for SUS 316 stainless steel in simulated PWR primary water at 320 C, J. Nucl. Sci.
657 Technol. 42 (2005) 225–232.
658 [37] D. Cubicciotti, Potential-pH diagrams for alloy-water systems under LWR conditions, J.
659 Nucl. Mater. 201 (1993) 176–183.
660 [38] Z. Zhu, X. Liu, Z. Ye, J. Zhang, F. Cao, J. Zhang, A fabrication of iridium oxide film pH micro-
661 sensor on Pt ultramicroelectrode and its application on in-situ pH distribution of 316L
662 stainless steel corrosion at open circuit potential, Sens. Actuators B Chem. 255 (2018)
663 1974–1982.
664 [39] Y. Zhao, X. Li, C. Zhang, T. Zhang, J. Xie, G. Zeng, D. Xu, F. Wang, Investigation of the
665 rotation speed on corrosion behavior of HP-13Cr stainless steel in the extremely
666 aggressive oilfield environment by using the rotating cage test, Corros. Sci. 145 (2018)
667 307–319.
668 [40] E. Van Hunnik, B.F. Pots, E. Hendriksen, The formation of protective FeCO3 corrosion
669 product layers in CO2 corrosion, NACE International, Houston, TX (United States), Paper
670 No. 6, 1996.
671 [41] M. Gao, X. Pang, K. Gao, The growth mechanism of CO2 corrosion product films, Corros.
672 Sci. 53 (2011) 557–568.
673 [42] W. Sun, S. Nešic, Kinetics of corrosion layer formation: part 1—iron carbonate layers in
674 carbon dioxide corrosion, Corrosion. 64 (2008) 334–346.
675 [43] J. Bischoff, A.T. Motta, Oxidation behavior of ferritic–martensitic and ODS steels in
676 supercritical water, J. Nucl. Mater. 424 (2012) 261–276.
677 [44] J. Töpfer, S. Aggarwal, R. Dieckmann, Point defects and cation tracer diffusion in (CrxFe1-

678 x) 3- δO4 spinels, Solid State Ion. 81 (1995) 251–266.
679